ADVANCED FUNCTIONAL MATERIALS
www.afm-journal.de

Gradient Bandgap-Tunable Perovskite Microwire Arrays toward Flexible Color-Cognitive Devices

Yue Fu, Meng Yuan, Yingjie Zhao, Meiqiu Dong, Yangwu Guo, Kui Wang, Chunqi Jin,* Jiangang Feng, Yuchen Wu, and Lei Jiang*

Color-cognitive detection plays an important role in many developing applications such as optical sensing, high-solution imaging, wearable biometric monitoring, and human visual cognitive system. Although color-cognitive devices have been demonstrated, the large size, complex manufacturing, high cost, and non-flexible processing impede their applications for distinguishing color information. Herein, gradient bandgap-tunable perovskite microwire arrays with excellent crystallinity and pure crystallographic orientation are realized by the synergy of the capillary-bridge assembly method and mild component engineering processing, yielding high-performance integrated color-cognitive devices with the spectral resolution of 14 nm ranging from 405 nm to 760 nm, responsivities over 10^3 A W^{-1}, and detectivities over 10^{15} Jones. Furthermore, the integrated flexible color-cognitive devices are demonstrated for accurately recognizing similar colors, which can be applied in color blindness correction. The efficient color recognition performances, together with the flexible processing, open new opportunities for the on-chip integration of wearable devices based on microwire arrays.

1. Introduction

Vision perception is an invaluable function that greatly bolsters diverse areas, ranging from security, and unmanned aerial vehicles, to biomedical imaging.[1–3] In particular, retina-inspired color perception systems further broaden the versatility of modern applications for color vision deficiency treatment, artificial intelligence, and autonomous driving.[4–7] Compared to the conventional charge-coupled device (CCD) equipped with optical filters and dichroic mirrors for color sensing, filter-free photodetectors show more advantages, such as accurate color perception, miniaturization, and simplified architecture.[5,8–10] Color-cognitive devices based on composition engineering CdS_xSe_{1-x} nanowires, silicon, and quantum dot (QD) arrays have been demonstrated, but relatively limited spectral response range, complicated fabrication processes, and non-flexible processing restrict their applications.[11–14] On the contrary, solution-processing materials offer an efficient path to constructing high-performance color recognition devices due to their large-area, low-cost, and flexible-substrate compatibility.[15–17]

As one of the typical solution-processing materials, perovskites have been widely used for visible light detection due to their superior optoelectronic properties, such as tunable bandgap, high charge carrier mobility, and low-cost facile production.[18–23] Efficient detection of optical information, such as intensity, polarization, and spectrum, enables boosting the development of scientific research and industrial processes.[22,24–33] Among them, the detection of light intensity and linear/circular polarization for perovskite devices has been extensively studied arising from the large chemical diversity of perovskites, but studies of color detection are still rare. Recently, spectrometer systems based on graded-bandgap perovskite thin films,

Y. Fu, M. Dong, Y. Guo, K. Wang, Y. Wu
Ji Hua Laboratory
Foshan, Guangdong 528200, P. R. China
M. Yuan, Y. Wu, L. Jiang
Key Laboratory of Bio-inspired Materials and Interfacial Science
Technical Institute of Physics and Chemistry
Chinese Academy of Sciences
Beijing 100190, P. R. China
M. Yuan
University of Chinese Academy of Sciences (UCAS)
Beijing 100049, P. R. China

The ORCID identification number(s) for the author(s) of this article can be found under https://doi.org/10.1002/adfm.202214094.

DOI: 10.1002/adfm.202214094

Y. Zhao
College of Chemistry
Zhengzhou University
Zhengzhou 450001, P. R. China
E-mail: zhaoyingjie5@zzu.edu.cn
C. Jin
GPL Photonics Lab
State Key Laboratory of Applied Optics
Changchun Institute of Optics
Fine Mechanics and Physics
Chinese Academy of Sciences
Changchun 130033, P. R. China
E-mail: chunqijin@ciomp.ac.cn
J. Feng
Division of Physics and Applied Physics
School of Physical and Mathematical Sciences
Nanyang Technological University
Singapore 637371, Singapore

perovskite microwires, and perovskite QD films have been realized by the spectral reconfiguration algorithm, which can accurately identify the spectrum over a wide range of wavelengths with high resolution.[34–39] Besides accurate identification of the spectrum information, the integrated flexible color-cognitive devices are also important due to their ability to meet the miniaturization and integration of wearable devices, but the device integration with the smaller footprint remains challenging.

In this work, we demonstrate high-performance integrated color-cognitive detectors enabling full spectral response (405-760 nm) with a spectral resolution of 14 nm based on gradient bandgap-tunable perovskite microwire arrays, which are fabricated by a combination of capillary-bridge assembly method and component engineering. Excellent crystallinity, pure crystallographic orientation, and accurate gradient bandgap along the microwires are demonstrated by X-ray diffraction (XRD), grazing-incidence wide-angle X-ray scattering (GIWAXS), and in situ spectral characterizations. These color sensing detectors exhibit excellent performance with responsivities over 10^3 A W^{-1}, and detectivities over 10^{15} Jones, which are 1–2 orders of magnitude higher than the corresponding polycrystalline thin films. Finally, the integrated flexible color-cognitive devices are demonstrated for color vision deficiency treatment, paving the way toward integrated wearable devices with a small footprint for color discrimination.

2. Results and Discussions

2.1. Color-Cognition Strategy

In combination with capillary bridges and composition engineering, high-performance color-cognitive devices were fabricated based on gradient bandgap-tunable perovskite microwire arrays. The device is designed and fabricated mainly considering the following three reasons. First, the 1D perovskite single-crystalline microwire arrays can be fabricated by a sandwich-type assembly system with an asymmetric-wettability topographical template, which can regulate the dewetting and crystallization process of the capillary bridge (Figure S1, Supporting Information, see details in the Experimental Section). The realization of high-quality microwire arrays can ensure lower noise levels due to suppressing the generation of defects, thus yielding high detectivity photodetectors (**Figure 1**a; Figure S2, Supporting Information, see details in the Experimental Section). Second, the synergy of the mild anion exchange and 1D microwire array structure is beneficial to the completion of the ion exchange reaction, and can well release the stress generated during the ion exchange process to prevent damage to the array structure (Figure 1b, see details in the Experimental Section). The gradient bandgap-tunable perovskite microwire arrays covering the whole visible spectrum can be prepared by regulating the anion exchange time (Figure 1c). Third,

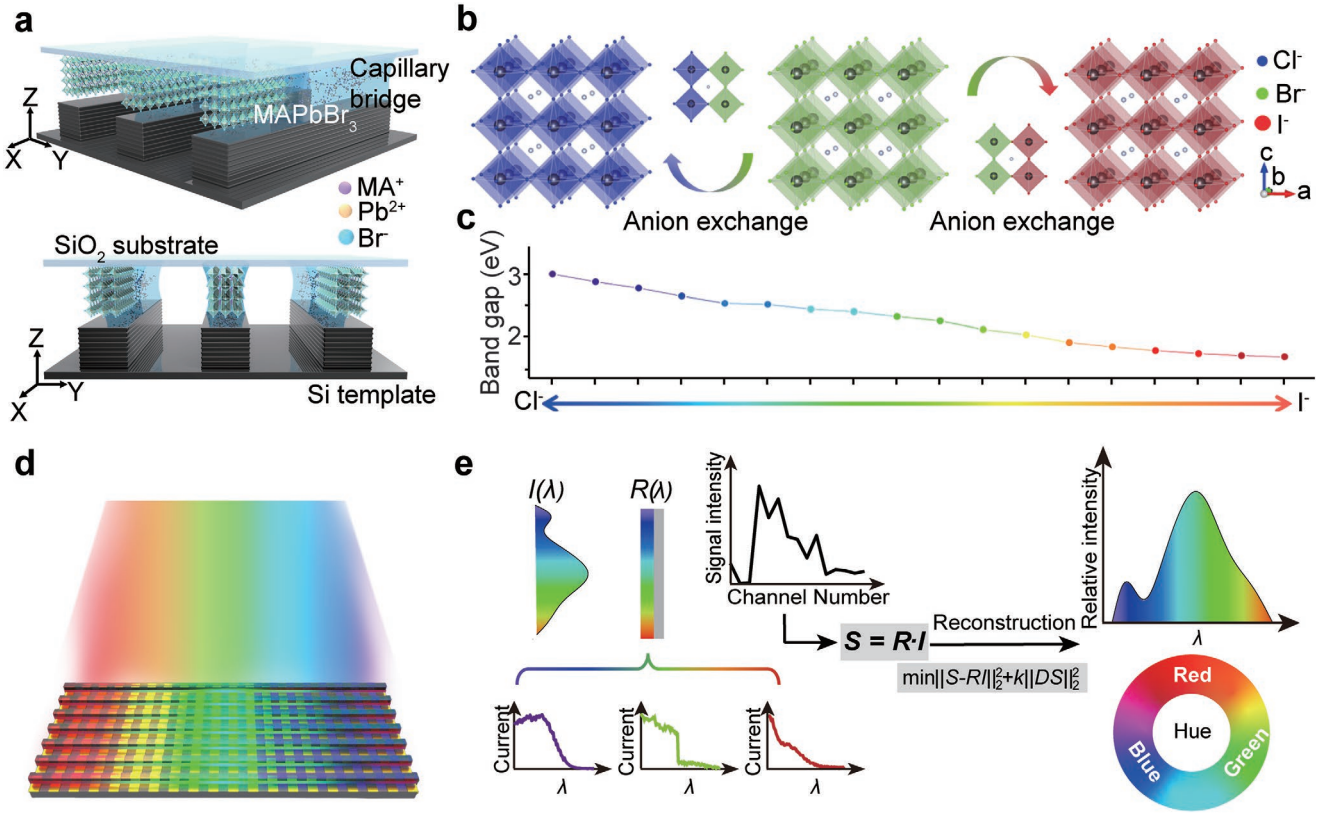

Figure 1. Conceptual design and schematics of gradient perovskite color-cognitive device. a) Schematic illustration of the fabrication of 1D single-crystalline microwire arrays. b) Schematic representation of the processes of halide exchange reactions. c) Gradient bandgap of perovskite 1D single-crystalline arrays as a function of anion exchange. d) Schematic of the optoelectronic device with gradient bandgap perovskite single-crystalline 1D arrays. e) The mechanism diagram of the final color perception.

high-performance color-cognitive devices can be fabricated by combining gradient bandgap-tunable perovskite microwire arrays with a computing algorithm (Figure 1d,e; Note S1, Supporting Information).

2.2. Characterizations of $MAPbX_3$ Microwire Arrays

To obtain the high-quality and gradient-bandgap methylammonium lead halides ($MAPbX_3$, X = Cl, Br, I) microwire arrays, we first develop an assembly method using an asymmetric-wettability topographical template to generate capillary bridges for patterning 1D $MAPbBr_3$ single-crystalline microwire arrays (Figures S2 and S3, Supporting Information, see details in the Experimental Section). In capillary bridges, the direction and position of capillary flows can inhibit the coffee-ring effect and control the growth position of perovskite crystals, resulting in the directional and site-specific growth of microwire arrays. The microwire arrays with pure orientation, high crystallinity, and homogeneous size can be generated after the exhaustion of solvents. The high uniform photoluminescence (PL) of long-range-ordered $MAPbBr_3$ single-crystalline assembly arrays demonstrates the homogeneity of the microwires (Figure S4, Supporting Information). To further assess the morphology, scanning electron microscopy (SEM) and the corresponding zoomed-in SEM images indicate 1D perovskite arrays with precise strict alignment, homogeneous size, smooth surface, and straight edge (Figure S5, Supporting Information). With the decreasing concentration of precursor solution, the width of the microwires decreases to 1.1 μm (Figure S6, Supporting Information, see details in the Experimental Section). The corresponding energy-dispersive X-ray spectroscopy (EDS) further demonstrates the homogenous atom distribution along with the arrays (Figure S7, Supporting Information). The pressure between the substrate and the micropillar template is a key role for control the height of the capillary bridge, which determines the height of the $MAPbBr_3$ single-crystalline microwire arrays (Figure S8, Supporting Information). The tunable thickness ranging from tens of nanometers to 1 micrometer enhances light absorption of microwires, achieves complete ion exchange, and promotes stress release during anion exchange.[40,41] The atomic force microscopy (AFM) images demonstrate the height of the microwire arrays change from 250 to 450 nm under the pressure from 0.7 MPa decreased to 0.5 MPa, (Figures S8 and S9, Supporting Information).

The synergistic effect of microwire arrays and the mild anion exchange reaction can avert the damage of the single crystal and the increase of defects. To achieve the controlled anion exchange reactions to prepare gradient-bandgap perovskite microwire arrays, composition engineering is applied by the micro-pulling technique. The $MAPbBr_3$ microwire arrays were used as the original material for gradient anion exchange, hence forming the microwire arrays from $MAPbCl_3$ to $MAPbI_3$. The anion-exchange kinetics in halide perovskite is mainly attributed to their low defect formation energy and the high ion mobility in the lattice owing to the prevalence of vacancies. Although both chlorine and iodine exchange will affect the kinetic processes, their anion exchange velocity is different. Furthermore, the lattice size will be compressed/ expanded when the halide ion changes from Br to Cl/I. To maintain the high quality of the microwire arrays, the halogen conversion rate of $MAPbX_3$ needs to be precisely controlled. As a consequence, we keep a constant speed of 10 μm s^{-1} to pull it out from the oleylammonium halide (OAmX, X = Cl, I) solution with a concentration of 20 mg mL^{-1} to complete the anion exchange process (Figure S10, Supporting Information, see details in the Experimental Section).

To further evaluate the morphology of the perovskite microwire arrays after anion exchange, SEM and AFM were performed. The SEM image shows that the morphology of gradient band-gap $MAPbX_3$ microwire arrays is well-preserved upon chemical conversion (**Figure 2**a). The EDS elemental maps and line scan EDS further demonstrate the gradient distribution of elements on gradient-bandgap perovskite microwire arrays (Figures S11 and S12, Supporting Information). The mild reaction conditions are essential for maintaining the microwire morphology and are compatible with nanofabrication processes.[42] AFM measurements demonstrate the microwires with smooth surfaces and straight edges. The heights of the $MAPbCl_3$ and $MAPbI_3$ are 236 nm and 265 nm, respectively (Figure S13 and S14, Supporting Information). In comparison with the $MAPbBr_3$ microwire featuring a height of 254 nm, the transformation height can be attributed to the difference in the lattice constant after anion exchange ($MAPbBr_3$: $a = b = c = 5.926$ Å, $MAPbCl_3$: $a = b = c = 5.666$ Å, and $MAPbI_3$: $a = b = c = 6.272$ Å) (Figure S15, Supporting Information).[43] As shown in Figure S16, we also obtained the local electronic structure of gradient-bandgap perovskite microwire arrays by Scanning Kelvin probe force microscopy (KPFM), which indicates the surface potential variation between two ends of microwire arrays. The higher surface potential values indicate a shallower Fermi level in $MAPbCl_3$ relative to $MAPbBr_3$ microwire arrays, and opposite to $MAPbI_3$. The gradient fluorescence emission and uniform brightness further validate the successful fabrication of the gradient perovskite microwire arrays (Figure S17, Supporting Information).

To investigate the optical properties of gradient perovskite microwire arrays, absorption and PL spectroscopy were performed. The micro-area absorption spectra of the perovskite array at each position and the schematic illustration of the measurements are shown in Figures S17 and S18 (Supporting Information). The absorption edge varying from 405 nm to 770 nm after anion exchange demonstrates the continuously tunable bandgap of the as-obtained perovskite microwire arrays. The corresponding PL peaks of these microwires change from 405 to 767 nm, indicating the formation of gradient perovskite single-crystalline microwire arrays from $MAPbCl_3$ to $MAPbI_3$ (Figure 2b). Meanwhile, the single fluorescence emission peak proves the complete anion-exchange reaction and avoids the formation of core-shell structure, which can be attributed to the tiny width and height of the microwire array.[42] To evaluate the carrier dynamics, we compared the time-resolved PL spectra of perovskite microwire arrays (Figure S19, Supporting Information). The dynamics can be fitted by biexponential decay, yielding two components of the time constant, in which the shorter component corresponds to the trap-mediated recombination and the longer component corresponds to the free-carrier recombination, respectively. The carrier lifetimes of the

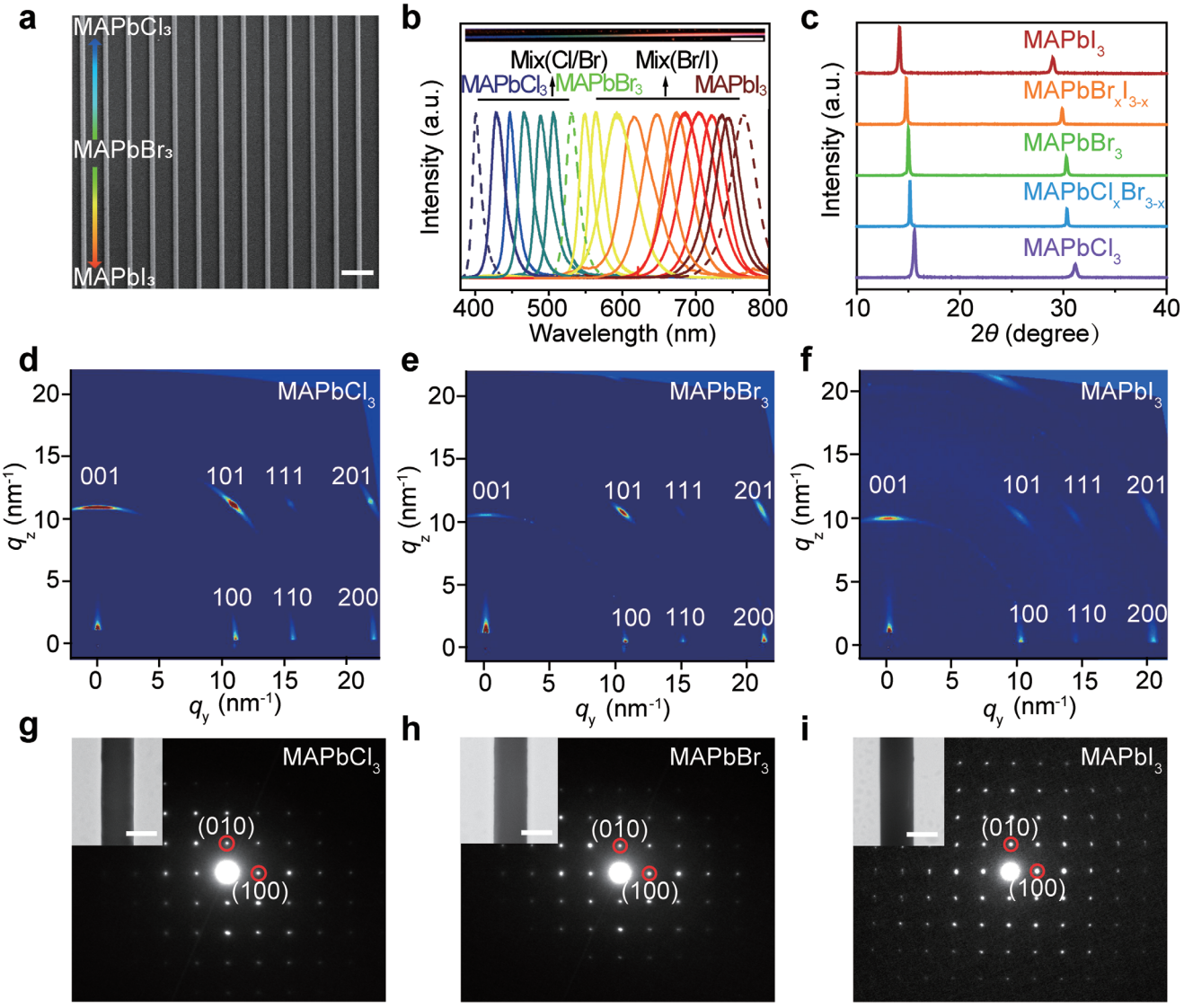

Figure 2. Characterization of high-quality gradient perovskite microwire arrays. a) SEM image of perovskite 1D single-crystalline heterojunction arrays with homogeneous sizes, precise positions, and strict alignment. Scale bar: 10 µm. b) Fluorescence micrograph of the typical compositionally graded $MAPbX_3$ microwire and the corresponding in situ fluorescence emission spectrum. Scale bar: 20 µm. c) XRD patterns of five typical states for perovskite single-crystalline arrays. d-f) GIWAXS patterns of perovskite single-crystalline 1D structure arrays of chloride exchanged $MAPbCl_3$, $MAPbBr_3$, and iodide exchanged $MAPbI_3$. g-i) TEM images and SAED patterns of perovskite single-crystalline 1D structure arrays of $MAPbCl_3$, $MAPbBr_3$, and $MAPbI_3$, depicting these microwires with a preferential (100) orientation in the growth direction. Scale bars: 1 µm.

microwire arrays are longer than that of corresponding films. Lower trap density and longer lifetimes indicate efficient photocarrier generation and transport, which is beneficial to the performance of optoelectronic devices. In addition, the completed exchanged $MAPbCl_3$ ($MAPbI_3$) and two-color heterojunction microwire arrays could also be fabricated (Figures S20 and S21, Supporting Information).

For characterization of the crystallinity and crystallographic orientation, XRD, GIWAXS, transmission electron microscopy (TEM), and selected area electron diffraction (SAED) measurements were performed. As shown in Figure 2c, the excellent crystallinity and pure crystallographic orientation of these perovskite microwires were demonstrated by XRD with sharp characteristic peaks, and noticeable peak position differences can be distinguished among $MAPbX_3$ perovskite microwire arrays. The increased ratio of Cl^-/Br^- will decrease the interplanar spacing while the increased ratio of I^-/Br^- will increase the interplanar spacing as evidenced by the peak shift in XRD. As shown in Figure 2d–f, and Figure S22, the preferential crystallographic orientations of perovskite microwire arrays were further characterized by GIWAXS. The discrete Bragg diffraction spots further illustrate that all perovskite microwire arrays are pure (001) crystallographic orientations with high crystallinity. TEM and SAED were carried out to determine the single crystallinity and the growth direction of perovskite microwire arrays. TEM images display smooth surfaces and the sharp edge of perovskite microwires (inset of Figure 2g–i). The SAED patterns suggest the preferred [010] growth direction of these

single-crystalline microwires (Figure 2g–i). We also measured TEM images and SAED patterns of microwire arrays in different areas of our devices to verify the single crystallinity of microwire arrays (Figure S23, Supporting Information). Therefore, combining the capillary-bridge approach with a mild anion-exchange reaction guarantees the fabrication of single-crystalline and pure-oriented gradient perovskite microwire arrays.

2.3. Photodetectors Performance of $MAPbX_3$ Microwire Arrays

Based on large-scale production of high-quality single-crystal microwire arrays, laterally configured photodetectors were fabricated on the SiO_2/Si substrate to investigate the photodetection performance. The logarithmic current-voltage curves present low dark currents and considerable photocurrents, which can be attributed to the excellent crystallinity of gradient perovskite microwire arrays (Figure S24, Supporting Information). The extremely low dark current provides a low noise level for achieving high detectivity. Evaluation of photodetection performance requires two important figures of merit, consisting of responsivity and detectivity. To evaluate the responsivity and specific detectivity, noise currents and frequency-modulated photocurrents under 5 V bias were measured (Figure S25, Supporting Information). Within the low-frequency region, the noise currents are dependent on the frequency, indicating that the noise currents are determined by $1/f$ noise (**Figure 3**a). At the high-frequency region, the average noise level is extremely low which approaches the shot-noise limit, $I_{shot} = (2eI_{dark})^{1/2}$, where e is the elementary charge and I_{dark} is the dark current. Figure 3b presents the irradiance-dependent photocurrents and responsivities of microwire devices at a modulation frequency of 30 Hz under a 405 nm light-emitting diode (LED) illumination. The photocurrent and the responsibility curves with different input power ranging from 2.5×10^{-6} to 128.2 mW cm^{-2} under the 405 nm illumination all show linear power dependence. The linear dynamic range (LDR) is a crucial parameter for photodetectors, which is expressed as LDR = 20 log (P_{sat}/P_{low}), where P_{sat} and P_{low} represent the highest and lowest incident light power within the fitted solid line. The devices exhibit an LDR of 154 dB due to the suppressed dark currents and considerable photocurrents. The responsivity R can be calculated by $R = I_{photo}/P$, where the photocurrent, I_{photo}, can be defined as $I_{photo} = I_{light} - I_{dark}$, I_{light}, and I_{dark} are the currents under illumination and dark, respectively. With the incident power increasing, the responsivities of three typical perovskite microwires show a reduced value due to the reduced photocarrier lifetime under high illumination power. The relationship between the normalized response and the input frequency of devices with perovskite microwires is shown in Figure 3c. The frequency response of devices with $MAPbBr_3$ perovskite

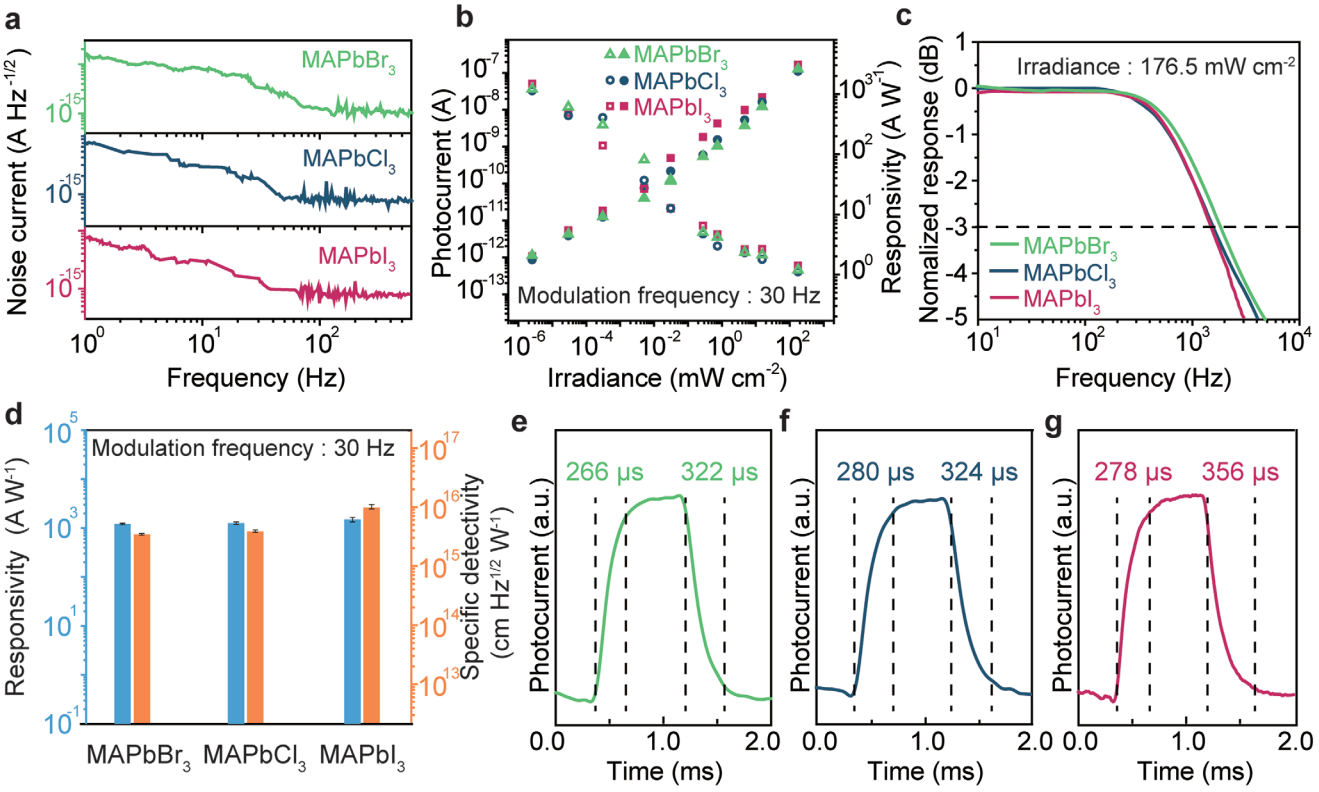

Figure 3. Device performance of gradient $MAPbX_3$ perovskite microwire arrays photodetectors. a) Frequency-dependent noise currents of microwire devices in the dark at 5 V bias. b) The irradiance-dependent photocurrents and responsivities of $MAPbX_3$ perovskite microwire array devices at a modulation frequency of 30 Hz under 405 nm LED illumination. c) Normalized response of $MAPbX_3$ perovskite microwire arrays at various frequencies. d) Statistics of responsivities and detectivities of $MAPbX_3$ perovskite microwire arrays under a modulation frequency of 30 Hz. The error bars represent the standard deviation. e–g) Temporal response of $MAPbX_3$ perovskite microwire arrays under a fixed illumination power of 120.5 mW cm^{-2}.

microwires relative to the pulse frequency shows a fast photoresponse of 3 dB cutoff frequency up to 1900 Hz, which is in good accordance with faster response speed because of good crystalline character. To evaluate the average responsivities and detectivities of each device, we assessed the statistics of device performances by measuring frequency-modulated photocurrents from 10 different devices under their lowest achievable irradiances (Figure S26, Supporting Information). Specific detectivity can be defined as $D^* = R(AB)^{1/2}/i_{noise}$, where A is the operating area of the device, B is the bandwidth and i_{noise} is the noise current. The average responsivities and detectivities at 30 Hz are shown in Figure 3d. The high D^* of $MAPbBr_3$, $MAPbCl_3$, and $MAPbI_3$ are 3.42×10^{15}, 3.84×10^{15}, and 9.77×10^{15} Jones (cm $Hz^{1/2}$ W^{-1}), corresponding to the responsivities of 1.21×10^3, 1.26×10^3, and 1.49×10^3 A W^{-1}, respectively. The temporal response of the photodetectors of perovskite microwire arrays is another important figure of merit (Figure 3e–g). The rise time is defined as the photocurrent increasing from 10% to 90% of the maximum photocurrent, and the decay time is opposed. The fast response rise time of $MAPbBr_3$ is 266 µs and the decay time is 322 µs under an irradiance of 120.5 mW cm^{-2} and 5 V bias. Multiple on-off cycles of photodetectors also indicate dependable device stability (Figure S27, Supporting Information). The XRD peak intensities of the typical three perovskite microwire arrays are almost unchanged under ambient conditions for 10 days, indicating the good environmental stability of the perovskite microwires (Figure S28, Supporting Information). For electric stability, the corresponding photodetectors under the 405 nm incident light can maintain good stability for 200 h (Figure S29, Supporting Information).

To highlight the significance of single-crystal perovskite microwire photodetectors, we carried out control experiments by fabricating photodetectors based on spin-coated thin film. The SEM images of the spin-coated thin film show a large number of grain boundaries and interfaces, indicating the high trap density and lower crystallinity, which is reflected by much weaker GIWAXS signals (Figure S30, Supporting Information). The photocurrents and responsivities of the $MAPbBr_3$ thin-film device are significantly lower than the single-crystalline microwire devices due to the carrier recombination and scattering at grain boundaries (Figure S31, Supporting Information).[15,16,23] These results demonstrate that eliminated grain boundaries and strict alignment of perovskite microwire arrays enable excellent optoelectronic performance.

2.4. On-Chip Integrated Color-Cognitive Device

In consideration of high-performance photodetectors based on the large-area gradient perovskite microwire arrays, we sought to demonstrate a miniaturization color-cognitive device with high resolution by computing algorithm.[37,44] **Figure 4**a shows four color-cognitive devices integrated on a SiO_2/Si substrate for color recognition. The single color-cognitive device consists of 23 independent photodetectors and every photodetector is defined between two neighboring electrodes as shown in Figure 4b. To work as a color cognitive device, arrays of different photodetectors produce different response spectra $R_i(\lambda)$, where λ is the incident wavelength. Thus, the measured signals of the device are as follows:[44]

$$S_i = \int I(\lambda)\, R_i(\lambda) d\lambda \quad (1)$$

where $I(\lambda)$ is the unknown spectrum, and $R_i(\lambda)$ can be characterized in experiments. Further details of the color-cognitive devices are given in the Experimental Section and Figures S32 and S33 (Supporting Information). To investigate the wavelength-dependent response curves of photodetectors along with the gradient perovskite microwire arrays, the photocurrent curves for 23 independent detectors were measured under different illumination wavelengths ranging from 400 to 760 nm with an interval of 14 nm (Figure 4c). By correlating photocurrents with different response ranges of gradient distribution along the length of the arrays using the computing algorithm, color-cognitive devices are attained (Note S1, Supporting Information). To evaluate the color recognition ability, color recognition tests were conducted for four different wavelengths of 430, 510, 590, and 650 nm with the full width at a half-maximum (FWHM) of 10 nm (Figure S34, Supporting Information). Figure 4d shows the reconstructed spectra based on our device (dotted lines) and the corresponding ideal spectra (solid lines) using the commercial instrument. All of the reconstructed spectra match well with the ideal spectra, demonstrating its excellent color recognition ability with high spectra resolution. Furthermore, monochromatic peaks across the 400–650 nm wavelength and broadband white light can also be reconstructed based on color-cognitive devices (Figure 4e,f). Meanwhile, a 14 nm spectral resolution is obtained as shown in Figure S35 (Supporting Information). The performance of our device has also been greatly improved compared to the previously published articles on perovskite spectrometers (Table S1, Supporting Information).

2.5. Flexible Color-Cognitive Device for Color Blindness Correction

Given that monochromatic and broadband spectra can be well reconstructed based on color-cognitive devices, we can help color vision-deficient (color blindness) patients to discriminate colors. Inspirited by the human visual system, we designed and integrated gradient bandgap-tunable perovskite microwire arrays on the flexible substrate for color cognition due to the compatibility with the needs of wearable devices (**Figure 5**a–c). Based on high-resolution monochromatic spectrum recognition, it can be beneficial for red-green blind patients to identify colors. In addition to red-green color blindness, blue blindness is another visual impairment in which patients are unable to recognize blue-violet colors and distinguish close colors. To verify the effect of the bending on the electrical signal, bending cycles and recorded current intensity were measured. No performance degradation was found after bending cycle tests, suggesting extremely stable properties of flexible devices (Figure 5d). As shown in Figure 5e, the flexible color-cognitive device exhibited an accurate spectrum and clear discrimination of similar blue colors from the color blindness test card. Both the strength and trend that we measured

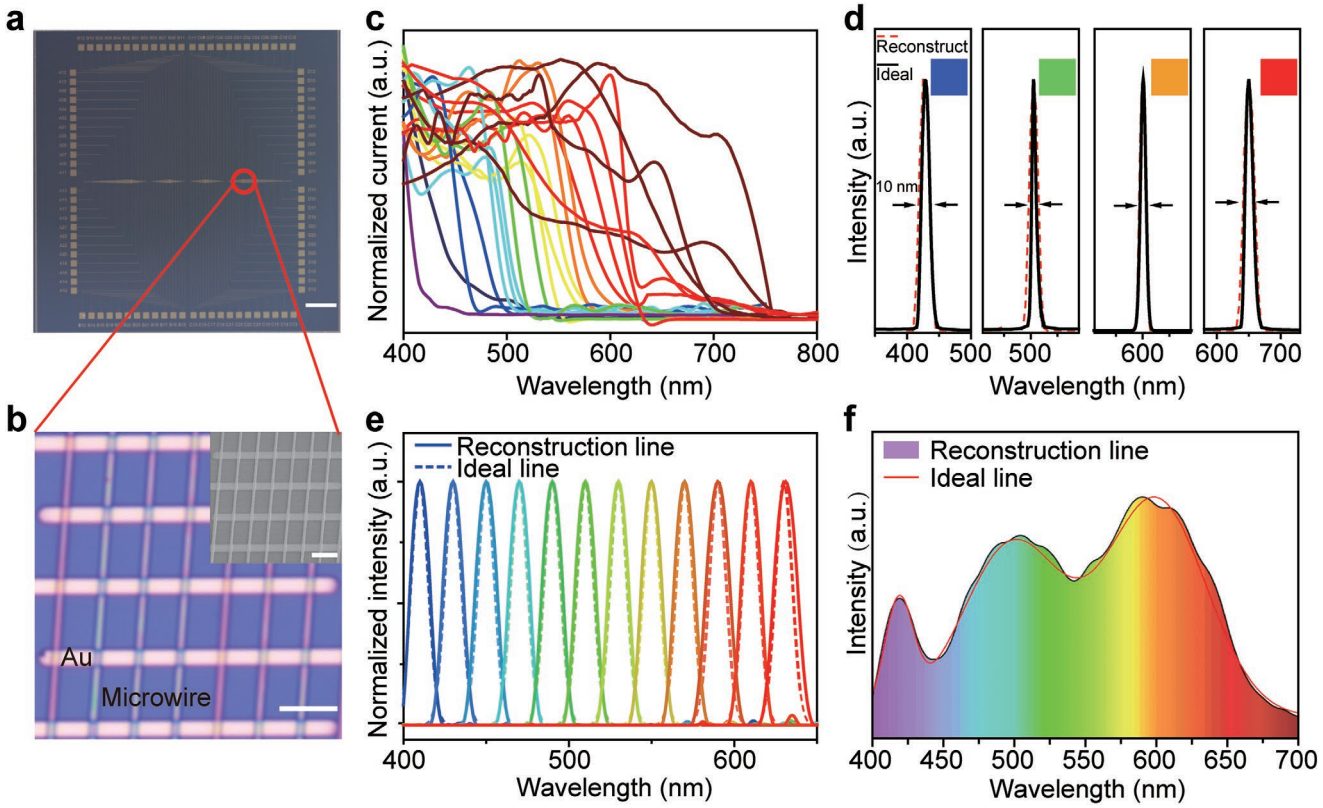

Figure 4. Monochromatic light detection. a) Photograph of the miniaturized spectrometer application based on perovskite single-crystalline arrays. scale bar: 2 mm. b) Optical microscopy image of photodetectors fabricated by the graded $MAPbX_3$ single-crystalline arrays, inset is the corresponding SEM image. Scale bars: 10 µm. c) The wavelength-dependent response curves of photodetectors on the graded perovskite single-crystalline microwire arrays. d) The reconstruction color spectrum (dotted line) using the miniaturized spectrometer and the ideal spectrum (solid line) of four different light sources. Arrows indicate FWHM. e,f) Simulated reconstruction spectrum by monochromatic peaks across the operational wavelength span and the broadband white light reconstructed using the color-cognitive device.

(dotted line) are highly consistent with ideal spectra (solid line). The measured and experimental spectra are also shown in the International Commission on Illumination (CIE) chromaticity diagram, demonstrating that the device is as good as the vision system in terms of similar color recognition (Figure 5f). Consequently, accurate color recognition not only can help color vision-deficient individuals to identify colors but also accelerate the development of artificial intelligence and autonomous driving.

3. Conclusion

In conclusion, color-cognitive devices based on gradient bandgap-tunable perovskite microwire arrays are realized by integrating the component engineering and capillary-bridge assembly technique. These detectors exhibit excellent color-cognitive performance with a spectral resolution of 14 nm (405–760 nm), responsivities over 10^3 A W^{-1}, and detectivities over 10^{15} Jones. Combining high-performance color recognition ability with flexible processing, the integrated flexible color-cognitive devices for color blindness correction are demonstrated, highlighting promising applications for the on-chip integration of wearable devices based on microwire arrays.

4. Experimental Section

Materials: Methylammonium bromide (MABr), lead bromide ($PbBr_2$), N, N-dimethylformamide (DMF), and dimethyl sulfoxide (DMSO), were all purchased from Sigma-Aldrich with no purification. Oleylammonium iodide (OAmI) and Oleylammonium chlorine (OAmCl) were purchased from Xi'an Polymer Light Technology Corp. 1-Octadecene (ODE) was purchased from Alfa Aesar.

Fabrication of $MAPbBr_3$ Single-Crystalline Microwire Arrays by an Asymmetric-Wettability Micropillar Assembly System: The perovskite precursor solution was prepared by solving 10 mg, 20 mg, and 30 mg of MABr and $PbBr_2$ with the same molar radio into 1 mL mixed solvents (50% DMSO and 50% DMF). Then, to fabricate $MAPbBr_3$ single-crystalline microwire arrays, a 7 µL precursor was dropped on a flat SiO_2/Si substrate, then covered by an asymmetric-wettability micropillar template with hydrophobic sidewalls and hydrophilic tops. The $MAPbBr_3$ single-crystalline microwire arrays can be acquired by placing the system in a vacuum oven at 70 °C for 8 h.

Fabrication of Gradient $MAPbX_3$ Microwire Arrays: To fabricate $MAPbBr_3$ – $MAPbCl_3$ gradient microwire arrays, 10 mg of OAmCl was dissolved in 10 mL ODE to make the conversion solution. The middle of $MAPbBr_3$ single-crystalline microwire arrays was immersed into the conversion solution at 40 °C for 16 h under the speed of 10 µm s^{-1} and then remain for 1.2 h between every movement under the control of the stepper motor. Then the chip was taken out of the solution and washed with chlorobenzene twice and hexanes once to remove the extra salts left on the chip. To fabricate $MAPbBr_3$ – $MAPbI_3$ gradient microwire arrays, 10 mg OAmI was dissolved in 10 mL ODE to make the conversion

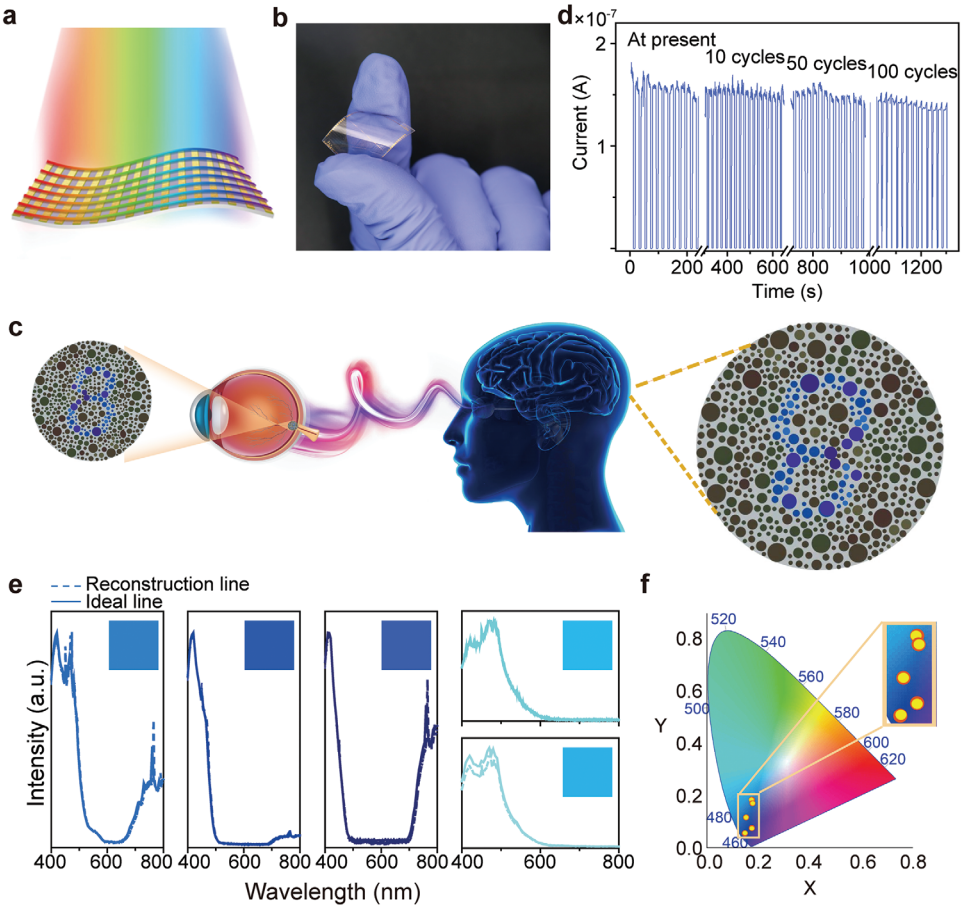

Figure 5. Demonstration of the flexible device and closely color-depending detection. a) Schematic diagram of the flexible color cognition device. b) Optical image of the flexible color cognition device. c) A schematic of colored perception capability of similar color image recognition in the human visual system. d) The bending test with different bending cycles of the $MAPbBr_3$ photodetector. e) Examples of five similar blue-color diagnosticity on object recognition via the flexible photodevices of perovskite 1D single-crystal arrays. f) The pigment perception presented on a CIEXYZ chromaticity diagram, the solid dots represent the pigment perceived by photodetectors and the hollow dots represent the pigment of the similar blue colors of the blind card.

solution and the reaction was carried out at 40 °C for 4 h under the speed of 10 µm s^{-1} and then remain 0.3 h between every movement under the control of stepper motor. The cleaning method is the same as above.

Characterizations: The morphology and element distribution of single-crystalline microwire arrays were performed by SEM (Hitachi, S-4800, Japan) at an accelerating voltage of 5.0 kV and a beam current of 10 µA. The AFM topography and surface potential (KPFM) were investigated by a Bruker MultiMode 8 Atomic Force Microscope. The crystallinity and pure orientation of different state XRD of anion-exchange $MAPbX_3$ were illustrated by JEOL TEM-2100 and X-ray diffractometer (Bruker, D8 focus, Germany) with monochromatized Cu K_α radiation ($\lambda = 1.5406$ Å). The GIWAXS patterns were collected at the Beijing Synchrotron Radiation Facility with an incidence angle of 0.2°. The in situ fluorescent micrographs were collected on an optical microscope (Vision Engineering Co., UK) integrated with a CCD camera. The micro-area optical absorption, PL emission spectra, and time-resolved photoluminescence of continued anion exchanged $MAPbX_3$ microwire array was obtained by microscopic confocal laser Raman spectrophotometer (Renishaw inViaReflex). Time-resolved photoluminescence spectra were carried out by Edinburgh Instruments FLS 980.

Device Fabrication and Measurements: Before fabricating $MAPbBr_3$ perovskite microwire arrays, the 300 nm SiO_2/Si wafer was cleaned sequentially with ethanol, acetone, and isopropanol, and then blown dry under a nitrogen gun. The 2 nm Cr and 50 nm Au as the bottom-electrode structure to form an ohmic connect were patterned by photolithography and thermally evaporating. The photoresist was spin-coated and exposed to UV light using an ABM/6/350/NUV/DCCD/M Lithography contact aligner, and then developed using RZX-3083 developer. This is followed by the deposition of 2 nm of chromium and 50 nm of gold using a metal evaporator. Lift-off is performed by immersion of the samples in acetone: isopropanol (3:1) mixture for 2 h. A structure of the planar bottom-electrodes-perovskite was constructed with spacing between electrodes 10 µm and the width of the electrode 50 µm, while the length of the perovskite microwire in the photodetector is ≈270 µm. An effective area of every device is ≈ 30 μm^2 for perovskite microwires covered by a pair of electrodes. The electrical characteristics of the photodetectors were performed using a Keithley 4200 semiconductor characterization system with a manual probe station (Lake Shore) in a vacuum of 10^{-5} Torr at room temperature. The device was illuminated by a 405 nm LED (Thorlabs) with different incident power. The temporal response of photodetectors was measured by a digital oscilloscope (Tektronix DPO 4104). Frequency-modulated noise currents and photocurrents were characterized by a current amplifier (SR570) and a lock-in amplifier (SR860, Stanford Research Systems). The current that varied with wavelength was measured by a monochromator (Omni-λ, Zolix) coupled with a tungsten halogen lamp (GLORIA-T250A, Zolix) used to provide different wavelengths of light. The light power was calibrated by a silicon photodiode (S130C, Thorlabs).

Statistical Analysis: To evaluate the average responsivities and detectivities of each device based on $MAPbX_3$ perovskite microwire

arrays, the frequency response of ten different devices was measured. The average responsivities and detectivities at a modulation frequency of 30 Hz under a 405 nm LED illumination with an irradiance of 2.5×10^{-6} mW cm^{-2} are shown in Figure 3d. The standard deviation of ten samples represented the degree of dispersion of the responsivities and detectivities of devices based on $MAPbX_3$ perovskite microwire arrays (Figure S26, Supporting Information). The error bars represent the standard deviation.

Supporting Information

Supporting Information is available from the Wiley Online Library or from the author.

Acknowledgements

Y.F. and M.Y. contributed equally to this work. The authors acknowledge the National Natural Science Foundation (21988102, 51922012, 52173190, 21633014, 62134009 and 62121005), the Ministry of Science and Technology (MOST) of China (2017YFA0204504, 2018YFA0208502, and 2018YFA0704803), the Youth Innovation Promotion Association CAS (2018034), and Ji Hua Laboratory Science Program: grant no. X190251UZ190.

Conflict of Interest

The authors declare no conflict of interest.

Data Availability Statement

Research data are not shared.

Keywords

color cognition, component engineering, microwire arrays, perovskites, photodetectors

Received: December 2, 2022
Revised: December 15, 2022
Published online: January 2, 2023

[1] Y. H. Jung, B. Park, J. U. Kim, T.-i. Kim, *Adv. Mater.* **2019**, *31*, 1803637.
[2] H. L. Park, H. Kim, D. Lim, H. Zhou, Y. H. Kim, Y. Lee, S. Park, T. W. Lee, *Adv. Mater.* **2020**, *32*, 1906899.
[3] J. Jang, S. Ji, G. K. Grandhi, H. B. Cho, W. B. Im, J. U. Park, *Adv. Mater.* **2021**, *33*, 2008539.
[4] F. P. García de Arquer, A. Armin, P. Meredith, E. H. Sargent, *Nat. Rev. Mater.* **2017**, *2*, 16100.
[5] R. D. Jansen-van Vuuren, A. Armin, A. K. Pandey, P. L. Burn, P. Meredith, *Adv. Mater.* **2016**, *28*, 4766.
[6] Y. H. Jung, B. Park, J. U. Kim, T. I. Kim, *Adv. Mater.* **2019**, *31*, 1803637.
[7] C. Han, X. Han, J. Han, M. He, S. Peng, C. Zhang, X. Liu, J. Gou, J. Wang, *Adv. Funct. Mater.* **2022**, *32*, 2113053.
[8] Z. Lan, F. Zhu, *ACS Nano* **2021**, *15*, 13674.
[9] J. M. Pino, J. M. Dreiling, C. Figgatt, J. P. Gaebler, S. A. Moses, M. S. Allman, C. H. Baldwin, M. Foss-Feig, D. Hayes, K. Mayer, C. Ryan-Anderson, B. Neyenhuis, *Nature* **2021**, *592*, 209.
[10] S. Jiang, M. Guan, J. Wu, G. Fang, X. Xu, D. Jin, Z. Liu, K. Shi, F. Bai, S. Wang, P. Xi, *Adv. Photonics* **2020**, *2*, 036005.
[11] J. Meng, J. J. Cadusch, K. B. Crozier, *Nano Lett.* **2020**, *20*, 320.
[12] W. Hartmann, P. Varytis, H. Gehring, N. Walter, F. Beutel, K. Busch, W. Pernice, *Nano Lett.* **2020**, *20*, 2625.
[13] Z. Yang, T. Albrow-Owen, H. Cui, J. Alexander-Webber, F. Gu, X. Wang, T. C. Wu, M. Zhuge, C. Williams, P. Wang, A. V. Zayats, W. Cai, L. Dai, S. Hofmann, M. Overend, L. Tong, Q. Yang, Z. Sum, T. Hasan, *Science* **2019**, *365*, 1017.
[14] J. Kim, C. Jo, M. G. Kim, G. S. Park, T. J. Marks, A. Facchetti, S. K. Park, *Adv. Mater.* **2022**, *34*, 2106215.
[15] Y. Sun, X. Liu, W. Deng, X. Zhang, Z. Lu, Z. Chang, X. Fang, D. Wu, J. Jie, *Adv. Funct. Mater.* **2022**, *32*, 2112758.
[16] S. X. Li, Y. S. Xu, C. L. Li, Q. Guo, G. Wang, H. Xia, H. H. Fang, L. Shen, H. B. Sun, *Adv. Mater.* **2020**, *32*, 2001998.
[17] J. Li, J. Wang, J. Ma, H. Shen, L. Li, X. Duan, D. Li, *Nat. Commun.* **2019**, *10*, 806.
[18] S. D. Stranks, G. E. Eperon, G. Grancini, C. Menelaou, M. J. P. Alcocer, T. Leijtens, L. M. Herz, A. Petrozza, H. J. Snaith, *Science* **2013**, *342*, 341.
[19] Y. Lin, Y. Fang, J. Zhao, Y. Shao, S. J. Stuard, M. M. Nahid, H. Ade, Q. Wang, J. E. Shield, N. Zhou, A. M. Moran, J. Huang, *Nat. Commun.* **2019**, *10*, 1008.
[20] Y. Liu, Y. Zhang, Z. Yang, H. Ye, J. Feng, Z. Xu, X. Zhang, R. Munir, J. Liu, P. Zuo, Q. Li, M. Hu, L. Meng, K. Wang, D. M. Smilgies, G. Zhao, H. Xu, Z. Yang, A. Amassian, J. Li, K. Zhao, S. F. Liu, *Nat. Commun.* **2018**, *9*, 5302.
[21] D. Pan, Y. Fu, N. Spitha, Y. Zhao, C. R. Roy, D. J. Morrow, D. D. Kohler, J. C. Wright, S. Jin, *Nat. Nanotechnol.* **2021**, *16*, 159.
[22] L. Wang, Y. Xue, M. Cui, Y. Huang, H. Xu, C. Qin, J. Yang, H. Dai, M. Yuan, *Angew. Chem. Int. Ed.* **2020**, *59*, 6442.
[23] J. Li, Z. Han, Y. Gu, D. Yu, J. Liu, D. Hu, X. Xu, H. Zeng, *Adv. Funct. Mater.* **2020**, *31*, 2008684.
[24] Y. Chen, G. Chen, Z. Zhou, X. Li, P. Ma, L. Li, W. Yin, H. Zeng, G. Zou, *Adv. Funct. Mater.* **2021**, *31*, 2101966.
[25] D. Luo, T. Zou, W. Yang, B. Xiang, X. Yang, Y. Wang, R. Su, L. Zhao, R. Zhu, H. Zhou, T. P. Russell, H. Yu, Z. H. Lu, *Adv. Funct. Mater.* **2020**, *30*, 2001692.
[26] Q. Song, Y. Wang, F. Vogelbacher, Y. Zhan, D. Zhu, Y. Lan, W. Fang, Z. Zhang, L. Jiang, Y. Song, M. Li, *Adv. Energy Mater.* **2021**, *11*, 2100742.
[27] J. Li, J. Wang, J. Ma, H. Shen, L. Li, X. Duan, D. Li, *Nat. Commun.* **2019**, *10*, 806.
[28] Y. Peng, X. Liu, L. Li, Y. Yao, H. Ye, X. Shang, X. Chen, J. Luo, *J. Am. Chem. Soc.* **2021**, *143*, 14077.
[29] X. Wang, Y. Wang, W. Gao, L. Song, C. Ran, Y. Chen, W. Huang, *Adv. Mater.* **2021**, *33*, 2003615.
[30] M. K. Jana, R. Song, H. Liu, D. R. Khanal, S. M. Janke, R. Zhao, C. Liu, Z. Valy Vardeny, V. Blum, D. B. Mitzi, *Nat. Commun.* **2020**, *11*, 4699.
[31] Y. Zhao, Y. Qiu, J. Feng, J. Zhao, G. Chen, H. Gao, Y. Zhao, L. Jiang, Y. Wu, *J. Am. Chem. Soc.* **2021**, *143*, 8437.
[32] L. Li, X. Liu, Y. Li, Z. Xu, Z. Wu, S. Han, K. Tao, M. Hong, J. Luo, Z. Sun, *J. Am. Chem. Soc.* **2019**, *141*, 2623.
[33] D. Li, X. Liu, W. Wu, Y. Peng, S. Zhao, L. Li, M. Hong, J. Luo, *Angew. Chem. Int. Ed.* **2021**, *60*, 8415.
[34] X. L. Wang, Y. Chen, Y. Chu, W. J. Liu, D. W. Zhang, S. J. Ding, X. Wu, *ACS Appl. Mater. Interfaces* **2022**, *14*, 14455.
[35] C. Jo, J. Kim, J. Y. Kwak, S. M. Kwon, J. B. Park, J. Kim, G. S. Park, M. G. Kim, Y. H. Kim, S. K. Park, *Adv. Mater.* **2022**, *34*, 2108979.
[36] L. Guo, H. Sun, M. Wang, M. Wang, L. Min, F. Cao, W. Tian, L. Li, *Adv. Mater.* **2022**, *34*, 2200221.
[37] X. Xu, Z. Han, Y. Zou, J. Li, Y. Gu, D. Hu, Y. He, J. Liu, D. Yu, F. Cao, H. Zeng, *Adv. Mater.* **2021**, *34*, 2108408.

[38] X. Zhu, L. Bian, H. Fu, L. Wang, B. Zou, Q. Dai, J. Zhang, H. Zhong, *Light Sci. Appl.* **2020**, *9*, 73.
[39] C. Chen, L. Gao, W. Gao, C. Ge, X. Du, Z. Li, Y. Yang, G. Niu, J. Tang, *Nat. Commun.* **2019**, *10*, 1927.
[40] M. Liu, S. D. Verma, Z. Zhang, J. Sung, A. Rao, *Nano Lett.* **2021**, *21*, 8945.
[41] X. Hu, Z. Huang, X. Zhou, P. Li, Y. Wang, Z. Huang, M. Su, W. Ren, F. Li, M. Li, Y. Chen, Y. Song, *Adv. Mater.* **2017**, *29*, 1703236.
[42] L. Dou, M. Lai, C. S. Kley, Y. Yang, C. G. Bischak, D. Zhang, S. W. Eaton, N. S. Ginsberg, P. Yang, *Proc. Natl. Acad. Sci. USA* **2017**, *114*, 7216.
[43] D. H. Son, S. M. Hughes, Y. Yin, A. P. Alivisatos, *Science* **2004**, *306*,1009.
[44] Z. Wang, S. Yi, A. Chen, M. Zhou, T. S. Luk, A. James, J. Nogan, W. Ross, G. Joe, A. Shahsafi, K. X. Wang, M. A. Kats, Z. Yu, *Nat. Commun.* **2019**, *10*, 1020.